RSC Advances

PAPER

View Article Online
View Journal | View Issue

Cite this: *RSC Adv.*, 2018, **8**, 21444

A channel-structured Eu-based metal–organic framework with a zwitterionic ligand for selectively sensing Fe^{3+} ions†

Yong-Qing Huang, *[a] Huai-Ying Chen,[a] Yang Wang,[a] Yong-He Ren,[a] Zong-Ge Li,[a] Lu-Chao Li[a] and Yan Wang[b]

Received 1st April 2018
Accepted 8th June 2018

DOI: 10.1039/c8ra02809e

rsc.li/rsc-advances

A novel Eu-based MOF $[Eu(IMS1)_2]Cl\cdot 4H_2O$ (**1**) was successfully constructed based on a semi-rigid zwitterionic 1,3-bis(4-carboxylbenzyl)-imidazolium (IMS1) ligand, featuring a 3-fold interpenetrating dia net structure with a point symbol of 6^6 and charged permanent micropores. Considering its excellent luminescent property as well as thermal and chemical stability, complex **1** was explored as a potential sensor for detecting Fe^{3+} ions. The results show that complex **1** has a high sensitivity and selectivity for Fe^{3+} based on a 'turn-off' effect, for which the electrostatic interaction between Fe^{3+} ions and the inner surface of the micropores may play a critical role. The fluorescence quenching mechanism reveals that dynamic quenching and competitive adsorption between Fe^{3+} and **1** lead to the quenching effect of **1**.

Introduction

It is well known that environmental pollution is a very serious problem that we are currently facing. Recently, with the continuous activity of humans, more and more heavy metal ions and toxic organic molecules have been released into the environment in soil, water and air, threatening the health and life of animals and human beings by way of the food chain.[1] Among various pollutants, iron is a special element, being indispensable for all living systems at certain concentrations. However, both its deficiency and excess will cause various biological disorders like hepatic cirrhosis, endotoxemia, and hereditary hemochromatosis.[2]

To accurately detect iron, several analytical techniques have been developed like ICP-MS, FAAS and spectrophotometric detection.[3] Among these probing techniques, the method based on luminescent metal–organic frameworks (LMOFs) as fluorescent sensors, combining the advantages of MOFs and luminescence sensors, have attracted considerable attention due to high sensitivity, selectivity and non-destructive nature.[4] Compared with traditional luminescent organic conjugate molecules,[5] LMOFs as sensing materials have some advantages, such as crystalline nature, diverse and modifiable structures, permanent porosity, tunable band gaps and electronic structures, *etc.*[6] In this respect, Ln-based LMOFs have great potential as fluorescence probes due to their unique optical properties such as large stokes shift, high color purity and relatively long luminescence lifetime.[7] Most importantly, for Eu/Tb-based MOF sensors, the pink or green light can be easily observed under a UV lamp by naked eyes, benefitting the low cost quick detection by the 'turn-off' effect.[8] Up to now, many Eu/Tb-based MOFs have been reported as sensors for detecting cations, anions, small molecules, organic solvents and poisonous gases, *etc.*[7–9]

On the other hand, except for metal ions or clusters, selection of organic linkers is another important factor for detection performance improvement of Fe^{3+} ions. Generally, outstanding organic linkers with functional groups can strengthen host–guest interaction, triggering electron transfer and/or energy transfer, which is responsible for the fluorescence changes.[8,10] Therefore, for synthesis of Eu/Tb-based MOF sensors, the design/selection of organic ligands becomes particularly important. Zwitterionic carboxylate ligands, especially functional pyridinium and imidazolium ligands, have been widely employed as bridging ligands to construct MOFs, some of which have exhibited impressive potential applications based on their Lewis acidic property and interaction with guest molecules.[11] Moreover, pure zwitterionic ligands have displayed potential application as luminescent sensors for sensing Fe^{3+} ions.[12] Based on the above analysis and taken into account that zwitterionic ligand is capable of forever generating electrostatic field inside the channels, and then reinforcing the interaction between the Eu-based MOF probe and the Fe^{3+} ions, we designed and synthesized a new semirigid zwitterionic 1,3-

[a]*State Key Laboratory of Mining Disaster Prevention and Control Co-founded by Shandong Province and the Ministry of Science and Technology, College of Chemical and Environmental Engineering, Shandong University of Science and Technology, Qingdao 266590, China. E-mail: yqhuangskd@163.com*

[b]*School of Chemistry and Chemical Engineering, Anhui Key Laboratory of Functional Coordination Compounds, Anqing Normal University, Anqing 246011, China*

† Electronic supplementary information (ESI) available: PXRD patterns, TGA curves, Fluorescent spectra, UV/Vis spectra and X-ray crystallographic files for complex **1** in CIF format. CCDC 1821918. For ESI and crystallographic data in CIF or other electronic format see DOI: 10.1039/c8ra02809e

bis(4-carboxylbenzyl)-imidazolium (IMS1) ligand to construct Eu-based MOF.[13] In this work, we successfully gained a Eu(III)-based channel-structured MOF $[Eu(IMS1)_2]Cl\cdot 4H_2O$ (**1**) with high stability towards aqueous solution in a wide range of pH values, being a promising fluorescence probe for selectively detecting Fe^{3+} ions.

Experimental

Materials and methods

All reagents and chemicals are purchased from HEOWNS, which are used without further purification. The 1,3-bis(4-carboxylbenzyl)-imidazolium (IMS1) ligand was synthesized according to the previously reported method.[14] Elemental analyses (C, H, N) were carried out using a Perkin-Elmer 240C elemental analyser. Infrared spectra were recorded in the range of 4000–400 cm^{-1} on a Nicolet 380 FT-IR spectrometer with KBr Pellets. Powder X-ray diffraction (PXRD) were measured at room temperature using a Rigaku Ultima IV diffractometer with graphite monochromatic Cu Kα radiation ($\lambda = 0.15418$ nm) at 40 kV and 40 mA. Simulated powder patterns were based on single crystal data and calculated using the Mercury software.[15] Thermogravimetric analysis (TGA) was performed using a STA 409 PC thermal analyser under the nitrogen atmosphere with a heating rate of 10 °C min^{-1}. The luminescent spectra for complex **1** were recorded at ambient temperature using a Hitachi F-4600 FL spectrophotometer. UV/Vis spectra were obtained using a Hitachi UH4150 Spectrophotometer within 300–800 nm.

Synthesis of $[Eu(IMS1)_2]Cl\cdot 4H_2O$ (1)

A mixture of IMS1 (0.3 mmol, 125.4 mg), $Eu(NO_3)_3\cdot 6H_2O$ (0.15 mmol, 66.6 mg), CH_3CN (6 mL) and H_2O (7 mL) was sealed in a 20 mL Teflon-lined bomb and heated at 150 °C for 3 days. After cooling to room temperature at a rate of 3 °C h^{-1}, light yellow prismatic crystals were obtained. Yield: 78%. Anal. Calcd for $C_{38}H_{38}ClEuN_4O_{12}$: C, 49.07; H, 4.12; N, 6.02. Found: C, 49.10; H, 4.08; N, 6.07. IR (KBr, cm^{-1}): 3468 (m), 3140 (m), 3067 (m), 1617 (s), 1557 (s), 1532 (s), 1416 (vs), 1351 (s), 1183 (w), 1153 (s), 1019 (w), 859 (m), 814 (m), 787 (m), 746 (s), 612 (m), 561 (w), 425 (w).

X-ray crystallography

The diffraction data was collected on the Bruker Smart ApexII CCD diffractometer with graphite-monochromated Mo Kα radiation ($\lambda = 0.071073$ nm). Empirical absorption correction was applied to the data using the multi-scan program SADABS.[16] The structure was solved by direct method (SHELXS-97) and refined by the full-matrix least-square method on F^2 using the SHELXL-97 program.[17] The coordinates of all non-hydrogen atoms were refined anisotropically. All H atoms of IMS1 ligands were situated at theoretically calculated positions and refined using a riding model isotropically, whereas the H atoms of lattice water molecules have not been ascertained by difference Fourier. All calculations were performed using the SHELTXL crystallographic software package.[18] Details of the crystal parameters, data collections and refinements for **1** are summarized in Table 1. Selected bond lengths and angles with their estimated standard deviations are given in Table 2.

Results and discussion

Structural description

Complex **1** was obtained by the solvothermal reaction of $Eu(NO_3)_3\cdot 6H_2O$ and $H_2(IMS1)Cl$ in CH_3CN–H_2O (6 : 7, v/v) at 150 °C for 3 days as light yellow crystals, which was confirmed by EA, IR, TGA and single crystal X-ray diffraction. The phase purity of the bulk crystalline samples was independently verified by powder X-ray diffraction (PXRD) (Fig. S1, ESI†). Crystal structure analysis reveals that **1** crystallizes in the tetragonal $I4_1/a$ space group (Table 1) and features a 3-fold interpenetrating 3D framework with the $Eu_2(CO_2)_8$ clusters as 4-connected nodes. The crystallographic asymmetric unit of **1** is composed of half europium atom, one IMS1 ligand, half chloride ion and two lattice water molecules. Each Eu^{3+} ion, sitting on the 4_1 screw axis, bonds to six IMS1 ligands with O_8 donor set, showing a trigondodecahedron geometry as exhibited in Fig. 1. The average Eu–O bond distance is 2.418 Å, and the O–Eu–O bond angles range from 52.73(8)° to 152.95(9)° (Table 2).

The structure of **1** features dinuclear Eu^{3+} cores as four-connected tetrahedral topological nodes. Each dinuclear cluster is surrounded by eight bridging IMS1 ligands, accompanying with intermetallic distance of 4.1613(3) Å, similar to that of the reported complex $[Eu_2(Hsal)_8][Zn(phen)_3]\cdot(H_2sal)(H_2O)$.[19] As depicted in Fig. 1, two symmetry-related Eu^{3+} ions in each cluster are first interconnected *via* four bidentate bridging carboxyl groups from four different IMS1 ligands, forming a classical paddle-wheel dinuclear unit. Then, another

Table 1 Crystal data for complex **1**

Complex	**1**
Empirical formula	$C_{38}H_{38}ClEuN_4O_{12}$
Formula weight	930.13
Crystal system	Tetragonal
Space group	$I4_1/a$
a (Å)	24.0818(8)
b (Å)	24.0818(8)
c (Å)	13.5997(9)
α (°)	90
β (°)	90
γ (°)	90
V (Å^3)	7886.9(6)
Z	8
D_{calc} (g cm^{-3})	1.567
μ (mm^{-1})	1.725
T (K)	293
F (000)	3760
$2\theta_{max}$ (°)	55
Independent reflections	4533
Data/restraints/parameters	4533/0/258
R_{int}	0.0398
Goodness-of-fit on F^2	1.059
R_1, $wR_2{}^a$ ($I > 2\sigma(I)$)	0.0306, 0.0815
R_1, $wR_2{}^a$ (all data)	0.0412, 0.0870

^{a} $R_1 = \Sigma||F_o| - |F_c||/\Sigma|F_o|$; $wR_2 = \{\Sigma[w(F_o{}^2 - F_c{}^2)^2]/\Sigma[w(F_o{}^2)^2]\}^{1/2}$.

Table 2 Selected bond distances (Å) and angles (°) for complex **1**[a]

Eu(1)-O(2)#1	2.290(2)	Eu(1)-O(2)#2	2.290(2)
Eu(1)-O(1)	2.435(2)	Eu(1)-O(1)#3	2.435(2)
Eu(1)-O(4)#4	2.443(2)	Eu(1)-O(4)#5	2.443(2)
Eu(1)-O(3)#5	2.503(2)	Eu(1)-O(3)#4	2.503(2)
O(2)#1-Eu(1)-O(2)#2	107.04(13)	O(2)#1-Eu(1)-O(1)	77.92(9)
O(2)#2-Eu(1)-O(1)	83.97(9)	O(2)#1-Eu(1)-O(1)#3	83.97(9)
O(2)#2-Eu(1)-O(1)#3	77.92(9)	O(1)-Eu(1)-O(1)#3	149.34(11)
O(2)#1-Eu(1)-O(4)#4	152.95(9)	O(2)#2-Eu(1)-O(4)#4	90.05(9)
O(1)-Eu(1)-O(4)#4	125.69(8)	O(1)#3-Eu(1)-O(4)#4	79.22(8)
O(2)#1-Eu(1)-O(4)#5	90.05(9)	O(2)#2-Eu(1)-O(4)#5	152.95(9)
O(1)-Eu(1)-O(4)#5	79.22(8)	O(1)#3-Eu(1)-O(4)#5	125.70(8)
O(4)#4-Eu(1)-O(4)#5	82.87(13)	O(2)#1-Eu(1)-O(3)#5	78.76(9)
O(2)#2-Eu(1)-O(3)#5	149.83(9)	O(1)-Eu(1)-O(3)#5	125.88(8)
O(1)#3-Eu(1)-O(3)#5	73.24(8)	O(4)#4-Eu(1)-O(3)#5	76.19(9)
O(4)#5-Eu(1)-O(3)#5	52.73(8)	O(2)#1-Eu(1)-O(3)#4	149.83(9)
O(2)#2-Eu(1)-O(3)#4	78.76(9)	O(1)-Eu(1)-O(3)#4	73.24(8)
O(1)#3-Eu(1)-O(3)#4	125.88(8)	O(4)#4-Eu(1)-O(3)#4	52.73(8)
O(4)#5-Eu(1)-O(3)#4	76.19(9)	O(3)#5-Eu(1)-O(3)#4	111.45(11)

[a] Symmetry transformations used to generate equivalent atoms: #1 $y+3/4, -x+5/4, -z+5/4$; #2 $-y+5/4, x-3/4, -z+5/4$; #3 $-x+2, -y+1/2, z+0$; #4 $-x+3/2, -y+1/2, -z+1/2$; #5 $x+1/2, y, -z+1/2$.

four IMS1 ligands are bound to dinuclear Eu^{3+} core by four bidentate chelating carboxyl groups. In other words, each IMS1 ligand takes μ_3-bridging mode to connect three Eu^{3+} ions: one carboxyl group take μ_2-κ^1O:κ^1O *syn–syn* bridging mode to link two Eu^{3+} ions and the other adopts chelating mode to coordinate to another Eu^{3+} ion. In fact, in terms of topological viewpoint, each μ_3-bridging IMS1 ligand can be regarded as 2-connected linker and, at the same time, each dinuclear Eu^{3+} core as a whole can be considered as a node.

On the other hand, the semirigid IMS1 ligands in **1** adopt *cis*-configuration, which means that two rigid arms are on the same side of the imidazole ring. As displayed in Fig. 1, two dinuclear cores together with two bent IMS1 ligands make up a M_4L_2 hexagon metallacycle with chair conformation. That is, although each cluster possesses eight bridging IMS1 ligands, sticking out for inter-cluster connection, it actually link with four same clusters by 'double bridges' with intercluster distance of 15.7803(5) Å and can be regarded as 4-connected tetrahedral node (Fig. 1 and 2). Apparently, the 3D framework of **1** can be simplified as usual dia net with a point symbol 6^6.[20] It is noticeable that the single real network of **1** exhibits four types of channel along three axis orientations. As shown in Fig. 2, there are identical two types of porthole (denoted as A and B) along *a*- and *-b* axis. Similarly, another two types of channel (denoted as C and D) exist along *c*-axis, which are parallel to 4_1 screw axis.

As we all know, the nature hates vacuum for large interface energy. The solid materials, including MOFs, with large vacancy, usually accommodate guest molecules or adopt interpenetration to reduce the free space. Unfortunately, the same thing occurs for compound **1**, even if bulky dinuclear Eu^{3+} clusters together with double bridges fail to prevent interpenetration. At last, **1** presents

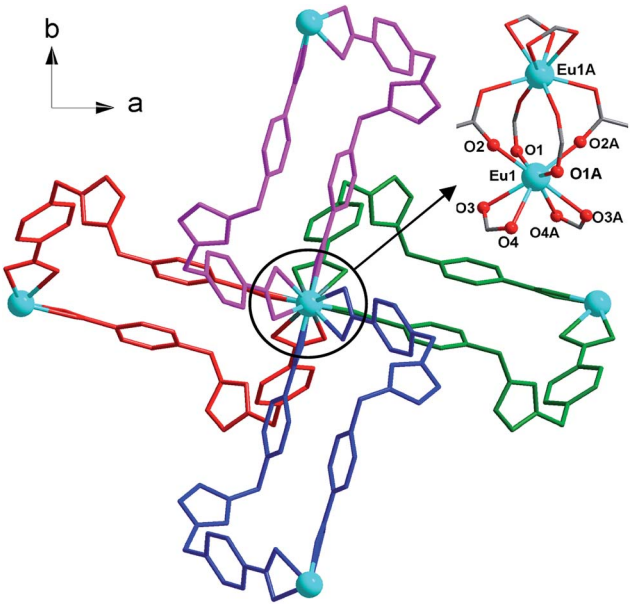

Fig. 1 Partial structure of **1**, showing the coordination environment of Eu(III) and linking fashion of dinuclear Eu(III) clusters. The hydrogen atoms, chloride ions and water molecules were omitted for clarity.

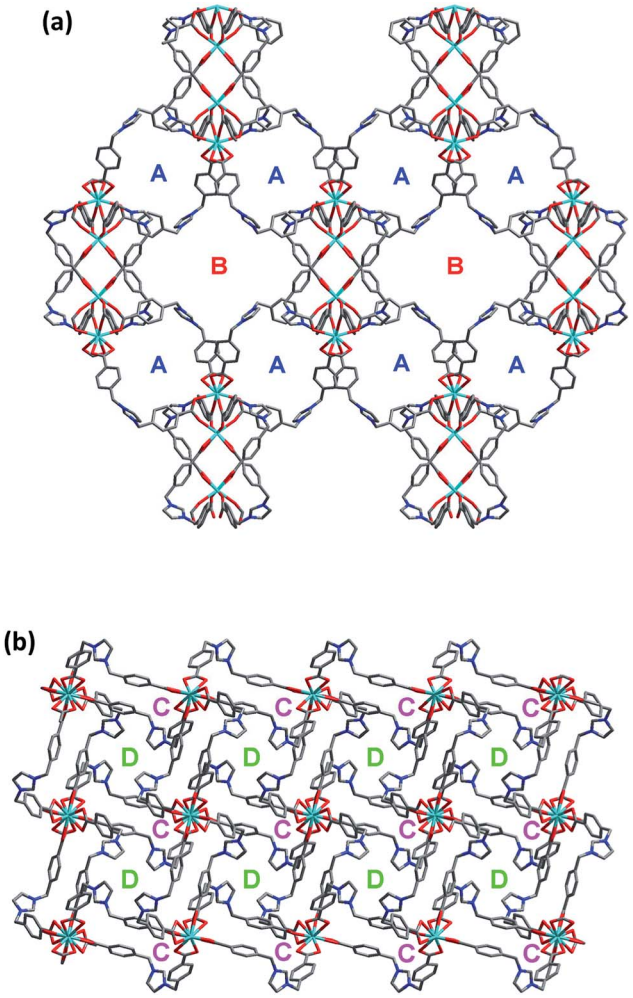

Fig. 2 The wire drawing of single diamondoid network of complex **1** along *a*- or *b*-axis (a) and *c*-axis (b), showing four types of channels. The hydrogen atoms, chloride ions and water molecules were omitted for clarity.

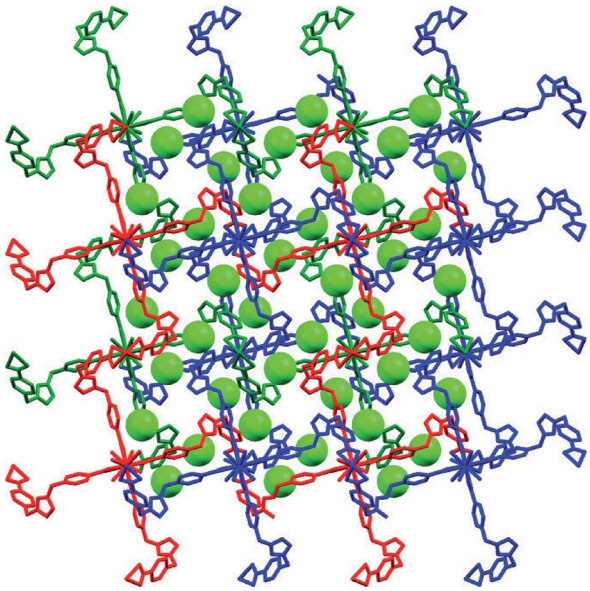

Fig. 3 The 3-fold interpenetrating diamondoid framework in **1**, showing chloride anions (green spheres) occupy C-type channels along *c*-axis. The guest water molecules occupying D-type channels and hydrogen atoms were omitted for clarity.

a 3-fold interpenetrating structure (Fig. 3). Notably, the nodes of three independent nets are aligned and equally spaced along 4_1 screw axis with the translation of 13.6 Å, equal to the length of *c*-axis. Additionally, the M_4L_2 macrocycles remain independent without catenation. Based on this common interpenetration mode, the channels running parallel to *a*- and *b*-axis direction disappear. In contrast, the D-type channels along *c*-axis orientation remain with cross-section of 5.95 × 5.95 $Å^2$ and are filled with guest water molecules. At the same time, the C-type channels are blocked up by counter chloride anions. It is noticeable that after removal of these guest water molecules in the voids, the effective free volume calculated using PLATON is still approximately 11.4% (896.4 $Å^3$ out of the 7886.9 $Å^3$ per unit cell volume).[21]

Thermo and chemical stability

To evaluate the thermal stability for further utilization, thermogravimetric analysis (TGA) of **1** was carried out under flowing N_2 atmosphere with the temperature range from 30 to 800 °C. The TGA curve displays an incessant weight loss of 7.29% in the low temperature region (<218.7 °C), which corresponds to the removal of lattice water molecules (calcd 7.74%) and the initial decomposition of the framework is observed up to *ca.* 350.7 °C, exhibiting excellent thermal stability. Needless to say, the high decomposition temperature of complex **1** is mainly attributed to the coordination bonding pattern and threefold interpenetrating structure, which solidified the flexible organic ligand. It is worth noting that, even if the as-synthesized complex **1** was dried under vacuum at 260 °C for 12 h, the crystalline water of **1** remains, which meaning that the guest water molecules are firmly confined in the cavity of **1** (Fig. S1 and S2, ESI†). On the other hand, the chemical stability of **1** in acidic, basic, and neutral aqueous solutions is very important for its practical application as Fe^{3+} sensor. So, we immersed the crystal samples of **1** into aqueous solutions with different pH values for 24 h to investigate its chemical stability. After filtering, the PXRD patterns of crystal samples are compared with the simulated one (Fig. S3, ESI†), which reveal that this material can maintain its crystallinity in aqueous solutions with pH values between 4 to 13. In one word, complex **1** has presented preeminent thermal and chemical stability, which lays a good foundation for its Fe^{3+} practical detection.

Luminescent sensing of Fe^{3+} ions

The solid-state fluorescence property of as-synthesized Eu-MOF **1**, as well as free H_2(IMS1)Cl ligand were both investigated at ambient temperature (Fig. S4, ESI†). The results show that complex **1** has strong characteristic emission at 594 nm and 618 nm upon maximum excitation at 395 nm, which can be attributed to the $^5D_0 \rightarrow {}^7F_1$ and $^5D_0 \rightarrow {}^7F_2$ transitions of Eu^{3+}, respectively. Apparently, the electric dipole transition emission at 618 nm is stronger than that of magnetic dipole moment transition at 594 nm, implying the Eu^{3+} ions of **1** in the tetragonal crystal system deviates from the center of symmetry in agreement with its crystal structure.[22] According to the excitation spectrum of **1**, the excitation maximum at 395 nm can be definitely attributed to $^7F_0 \rightarrow {}^5L_6$ transition of Eu^{3+} (Fig. S5, ESI†). On the other hand, the H_2(IMS1)Cl ligand exhibits the emission maximum at 397 nm upon the excitation at 340 nm, whereas there is no detectable luminescence when the excitation wavelength is 395 nm. It is worth noting that the emission intensity of complex **1** become weaker upon excitation at 340 nm than that upon excitation at 395 nm, and the emission peak arising from the free ligand disappears. As shown in Fig. S3 and S4, ESI,† the emission band of H_2(IMS1)Cl ligand and the excitation band of **1** is almost completely overlapping, indicating the existence of fluorescence resonance energy transfer (FRET) between the IMS1 ligands and coordinated Eu^{3+} ions.

Based on the microporous and permanent electrostatic field, we investigated the potential ability of complex **1** for sensing metal ions. First, 5 mg of crystalline samples of **1** were ground to powder, and then dispersed into 3 mL of water solution of MCl_x ($M = Mn^{2+}$, Ba^{2+}, Ca^{2+}, Co^{2+}, Cu^{2+}, Cd^{2+}, Ni^{2+}, Zn^{2+}, Hg^{2+}, Fe^{2+}, Al^{3+}, Cr^{3+}, Fe^{3+}) (0.1 M) for half an hour of ultrasonic oscillation, forming a series of suspension prior to fluorescence measurements. In contrast to the suspension of complex **1** in water, all suspensions with tested divalent and trivalent metal ions have different extent decrease of luminescence intensity. Among them, Ni^{2+}, Fe^{2+}, and Cr^{3+} ions display a big intensity reduction, while Fe^{3+} ion exhibit the drastic quenching effect on the luminescence of **1**, accompanied with a remarkable luminescence quenching visible to the naked eye under UV lamp (Fig. 4). Further, competitive experiments demonstrate that the presence of other metal ions have no significant effect on the luminescence response induced by Fe^{3+} ion (Fig. S6, ESI†). Compared with **1**, the ligand H_2(IMS1)Cl also showed selective luminescence quenching response to Fe^{3+} ions in suspensions, but the quenching phenomenon can't be observed to naked eyes under UV lamp (Fig. S7, ESI†). These results preliminarily prove that the electrostatic forces may play a significant role for

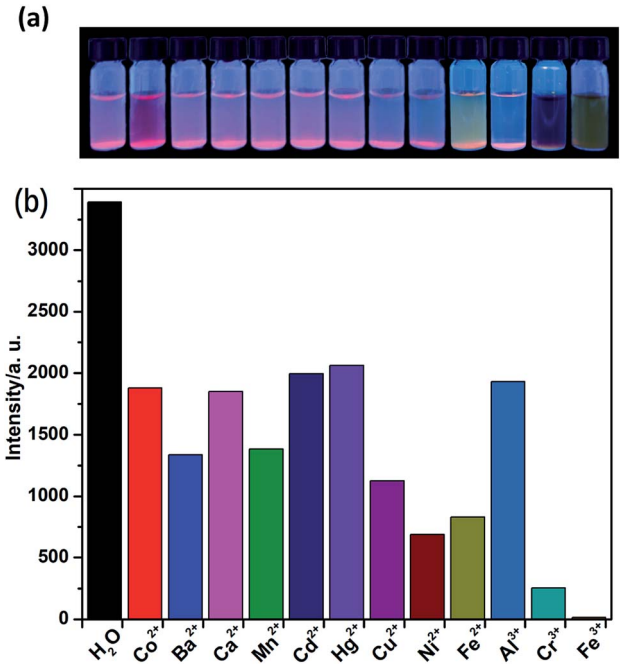

Fig. 4 (a) The picture of complex **1** in different metal ion solution at 365 nm UV light; (b) comparison of the luminescence intensity of **1** in different MCl_x aqueous solutions (0.1 M) upon excitation at 395 nm.

the detection of Fe^{3+} ions. To verify the basic framework of the complex **1** treated by the metal aqueous solutions, PXRD patterns were compared with the simulated one (Fig. S8, ESI†). The coincidence of calculated PXRD patterns with the experimental datum can rule out that the fluorescence quenching phenomena resulted from collapse of the framework of **1**.

Intrigued by the results, we prepared a series of Fe^{3+} aqueous solutions with molar concentration ranging from 1×10^{-6} to 1×10^{-1} M to further investigate the relationship between quenching effect, which was quantified by monitoring the emission spectral intensity of $^5D_0 \rightarrow {}^7F_2$ located in 618 nm, and the concentrations of Fe^{3+} ion. As shown in Fig. 5, the luminescence intensity of **1** decreased gradually as the concentration of Fe^{3+} ion increased. When the concentration reaches up to 1×10^{-1} M, the luminescence is completely quenched with 99.61% quenching efficiency. Meanwhile, the dose–response graph was well fitted by the Stern–Volmer equation in the concentration range of 1×10^{-6} to 1×10^{-3} M. As displayed in the inset of Fig. 5, a very good linear correlation ($R^2 = 0.99504$) was observed between the quenching efficiency and the amount of Fe^{3+} with high K_{SV} value of 5873.4 M^{-1}. Furthermore, the detection limit is calculated to be 2.3×10^{-5} mol L^{-1} (3.74 ppm) according to $3\delta/k$, where δ is standard error and k is slope. The high K_{SV} value and low detection limit, which are comparable to the reported values (Table. S1, ESI†), suggest that complex **1** is a powerful candidate for highly detective sensor for Fe^{3+} ions. On the other hand, the recyclability is one of the important indicator for sensors, which can effectively reduce the cost of practical application. Thus, the related experiments were conducted. Firstly, the crystal samples of **1** were soaked in the 0.1 M Fe^{3+} solution for minutes to form Fe^{3+}@ **1**. Then Fe^{3+}@ **1** was centrifuged and washed with water for three times. The results indicate that the luminescent intensity of recycled **1** was almost unchanged compared to initial value after five recycles (Fig. S9, ESI†). In the meantime, the PXRD patterns of recycled **1** ensure its structure unchangeable.

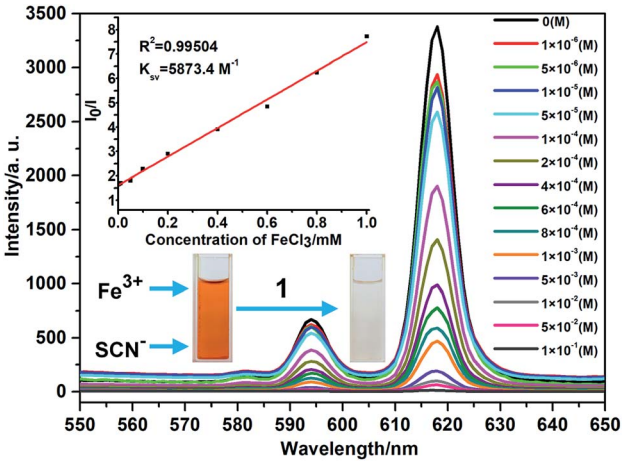

Fig. 5 The luminescence spectra of **1** with different concentration of Fe^{3+} ions. The inset shows that the dose–response graph at 618 nm, revealing the quenching effect and the concentration of Fe^{3+} ions and photo of $Fe(SCN)_3$ solution treated with complex **1**.

To explore the probable quenching reasons caused by Fe^{3+} ion, the UV-Vis absorption spectra of MCl_x aqueous solutions (1×10^{-4}), suspension of **1** in water, and suspension of **1** with Fe^{3+} in water were carried out, respectively (Fig. S11, ESI†). The results reveal that Fe^{3+} aqueous, suspension of **1**, and suspension of **1** with Fe^{3+} ions all have absorption at 395 nm. It is worth noting that the absorption ability of suspension of **1** with Fe^{3+} ions is stronger than the sum of Fe^{3+} and suspension of **1**, implying the presence of interaction between the charged internal surface of **1** and Fe^{3+} ions. To prove this point, **1** was added to the brown $Fe(SCN)_3$ solution, and then the solution quickly becomes colorless, further supporting the existence of strong host–guest interaction inside of the micropore. In addition, UV-Vis absorption spectrum of **1** with Fe^{3+} is similar to that of the Fe^{3+} aqueous. Based on the fact that, only in the low Fe^{3+} concentration range of 1×10^{-6} to 1×10^{-3} M, there is a good linear correlation between the I_0/I and the concentration of Fe^{3+}, as predicted by the Stern–Volmer law, quenching is considered entirely dynamic[23] below the concentration of 1×10^{-3} M, with a large Stern–Volmer constant of 5873.4 M^{-1}. On the contrary, beyond the concentration of 1×10^{-3} M, the luminescence quenching may arise from the competitive adsorption.[24] In other words, two types of quenching pathway coexist in a competitive manner with another, which factor playing the key role mainly depends on the Fe^{3+} concentration.

Conclusions

In summary, a new microporous Eu-MOF **1** with a semirigid zwitterionic IMS1 ligand was designed and synthesized, which displays excellent luminous performance and high chemical stability in aqueous solution with pH value between 4 to 13. Based on these merits together with permanent electrostatic field, the response ability of **1** for different metal ions in aqueous solution was investigated, and the results reveal that **1**

had high sensitivity and selectivity for Fe^{3+}. The fluorescence quenching mechanism indicates that dynamic quenching and competitive absorption between Fe^{3+} and **1** result in the quenching effect of **1**.

Conflicts of interest

There are no conflicts to declare.

Acknowledgements

This work was financially supported by the National Natural Science Foundation of China (Grant No. 21201111) and the Key Project of Anhui Provincial Fund for Distinguished Young Scholars in Colleges and Universities (No. 2013SQRL059ZD).

References

1 (*a*) L. Järup, *Br. Med. Bull.*, 2003, **68**, 167–182; (*b*) S. Cheng, *Environ. Sci. Pollut. Res.*, 2003, **10**, 192–198; (*c*) M. Hakim, Y. Y. Broza, O. Barash, N. Peled, M. Phillips, A. Amann and M. Haick, *Chem. Rev.*, 2012, **112**, 5949–5966; (*d*) J. L. Martinez, *Environ. Pollut.*, 2009, **157**, 2893–2902; (*e*) X. Zhang, X. Luo, N. Zhang, J. Wu and Y.-Q. Huang, *Inorg. Chem. Front.*, 2017, **4**, 1888–1894; (*f*) D. Han and M. J. Currell, *Sci. Total Environ.*, 2017, **580**, 602–625.

2 (*a*) L. L. Dunn, Y. S. Rahmanto and D. R. Richardson, *Trends Cell Biol.*, 2007, **17**, 93–100; (*b*) N. C. Andrews, *N. Engl. J. Med.*, 1999, **341**, 1986–1995; (*c*) F. O. Omara and B. R. Blakley, *J. Nutr.*, 1993, **123**, 1649–1655; (*d*) L. H. Allen, *J. Nutr.*, 2002, **132**, 813S–819S.

3 (*a*) L. S. Huang and K. C. Lin, *Spectrochim. Acta, Part B*, 2001, **56**, 123–128; (*b*) T. B. To, D. K. Nordstrom, K. M. Cunningham, J. W. Ball and R. B. McCleskey, *Environ. Sci. Technol.*, 1999, **33**, 807–813; (*c*) R. Ajlec and J. Stupar, *Analyst*, 1989, **114**, 137–142; (*d*) E. Chinoporos, *Anal. Chem.*, 1962, **34**, 437–438; (*e*) P. Wu, Y. Li and X. P. Yan, *Anal. Chem.*, 2009, **81**, 6252–5257; (*f*) Y.-T. Yan, J. Liu, G.-P. Yang, F. Zhang, Y.-K. Fan, W.-Y. Zhang and Y.-Y. Wang, *CrystEngComm*, 2018, **20**, 477–486.

4 (*a*) K. Müller-Buschbaum, F. Beuerle and C. Feldmann, *Microporous Mesoporous Mater.*, 2015, **216**, 171–199; (*b*) Z. Hu, B. J. Deibert and J. Li, *Chem. Soc. Rev.*, 2014, **43**, 5815–5840; (*c*) K. Jayaramulu, R. P. Narayanan, S. J. George and T. K. Maji, *Inorg. Chem.*, 2012, **51**, 10089–10091; (*d*) Y. Cui, Y. Yue, G. Qian and B. Chen, *Chem. Rev.*, 2012, **112**, 1126–1162.

5 (*a*) F. S. K. Sahoo, D. Sharma, R. K. Bera, G. Crisponi and J. F. Callan, *Chem. Soc. Rev.*, 2012, **41**, 7195–7227; (*b*) C. Pan, K. Wang, S. Ji, H. Wang, Z. Li, H. He and Y. Huo, *RSC Adv.*, 2017, **7**, 36007–36014; (*c*) B. B. Zhang, H. Y. Liu, F. X. Wu, G. F. Hao, Y. Z. Chen, C. Y. Tan, Y. Tan and Y. Y. Jiang, *Sens. Actuators, B*, 2017, **243**, 765–774; (*d*) J. Liu and Y. Qian, *J. Lumin.*, 2017, **187**, 33–39.

6 (*a*) Z.-F. Wu, L.-K. Gong and X.-Y. Huang, *Inorg. Chem.*, 2017, **56**, 7397–7401; (*b*) B. Parmar, Y. Rachuri, K. K. Bisht and E. Suresh, *Inorg. Chem.*, 2017, **56**, 10939–10949; (*c*) Z.-F. Wu and X.-Y. Huang, *Dalton Trans.*, 2017, **46**, 12597–12604; (*d*) J.-M. Zhou, W. Shi, H.-M. Li, H. Li and P. Cheng, *J. Phys. Chem. C*, 2014, **118**, 416–426; (*e*) J. Zhao, Y.-N. Wang, W.-W. Dong, Y.-P. Wu, D.-S. Li and Q.-C. Zhang, *Inorg. Chem.*, 2016, **55**, 3265–3271; (*f*) R. Lv, H. Li, J. Su, X. Fu, B. Yang, W. Gu and X. Liu, *Inorg. Chem.*, 2017, **56**, 12348–12356.

7 (*a*) S. Dang, E. Ma, Z. Sun and H. Zhang, *J. Mater. Chem.*, 2012, **22**, 16920–16926; (*b*) C. Yang, H. ren and X. Yan, *Anal. Chem.*, 2013, **85**, 7441–7446; (*c*) J. Hao and B. Yan, *J. Mater. Chem. C*, 2014, **2**, 6758–6764; (*d*) X. Song, S. Song, S. Zhao, Z. Hao, M. Zhu, X. Meng, L. Wu and H. Zhang, *Adv. Funct. Mater.*, 2014, **24**, 4034–4041; (*e*) T. W. Duan and B. Yan, *J. Mater. Chem. C*, 2014, **2**, 5098–5104.

8 (*a*) W. Yan, C. Zhang, S. Chen, L. Han and H. Zheng, *ACS Appl. Mater. Interfaces*, 2017, **9**, 1629–1634; (*b*) G.-P. Li, G. Liu, Y.-Z. Li, L. Hou, Y.-Y. Wang and Z. Zhu, *Inorg. Chem.*, 2016, **55**, 3952–3959; (*c*) M. Zhang, J. Han, H. WU, Q. Wei, G. Xie, S. Chen and S. Gao, *RSC Adv.*, 2016, **6**, 94622–94628; (*d*) X.-L. Zhao, D. Tian, Q. Gao, H.-W. Sun, J. Xu and X.-H. Bu, *Dalton Trans.*, 2016, **45**, 1040–1046.

9 (*a*) H. Li, Y. Han, Z. Shao, N. Li, C. Huang and H. Hou, *Dalton Trans.*, 2017, **46**, 12201–12208; (*b*) J. Wang, M. Jiang, L. Yan, R. Peng, M. Huangfu, X. Guo, Y. Li and P. Wu, *Inorg. Chem.*, 2016, **55**, 12660–12668; (*c*) Z. Hao, X. Song, M. Zhu, X. Meng, S. Zhao, S. Su, W. Yang, S. Song and H. Zhang, *J. Mater. Chem. A*, 2013, **1**, 11043–11050; (*d*) S. Xing, Q. Bing, L. Song, G. Li, J. Liu, Z. Shi, S. Feng and R. Xu, *Chem. –Eur. J.*, 2016, **22**, 16230–16235; (*e*) Z.-Q. Liu, Y.-Q. Huang and W.-Y. Sun, *Chin. J. Inorg. Chem.*, 2017, **33**, 1959–1969; (*f*) D. Tian, Y. Li, R.-Y. Chen, Z. Chang, G.-Y. Wang and X.-H. Bu, *J. Mater. Chem. A*, 2014, **2**, 1465–1470; (*g*) D. Tian, X.-J. Liu, R. Feng, J.-L. Xu, J. Xu, R.-Y. Chen, L. Huang and X.-H. Bu, *ACS Appl. Mater. Interfaces*, 2018, **10**, 5618–5625.

10 (*a*) S. Pal and P. K. Bharadwaj, *Cryst. Growth Des.*, 2016, **16**, 5852–5858; (*b*) Q. Tang, S. Liu, Y. Liu, J. Miao, S. Li, L. Zhang, Z. Shi and Z. Zheng, *Inorg. Chem.*, 2013, **52**, 2799–2801; (*c*) M.-L. Han, G.-W. Xu, D.-S. Li, L. M. Azofra, J. Zhao, B. Chen and C. Sun, *ChemistrySelect*, 2016, **1**, 3555–3561; (*d*) L.-H. Liu, X.-T. Qiu, Y.-J. Wang, Q. Shi, Y.-Q. Sun and Y.-P. Chen, *Dalton Trans.*, 2017, **36**, 12106–12113.

11 (*a*) M. Higuchi, K. Nakamura, S. Horike, Y. Hijikata, N. Yanai, T. Fukushima, J. Kim, K. Kato, M. Takata, D. Watanabe, S. Oshima and S. Kitagawa, *Angew. Chem., Int. Ed.*, 2012, **51**, 8369–8372; (*b*) Y.-Q. Huang, Z.-G. Li, H.-Y. Chen, H.-D. Cheng, Y. Wang, Y.-H. Ren, Y. Zhao and L. Liu, *CrystEngComm*, 2017, **19**, 6686–6694; (*c*) Y.-Q. Huang, H.-D. Cheng, H.-Y. Chen, Y. Wan, C.-L. Liu, Y. Zhao, X.-F. Xiao and L.-H. Chen, *CrystEngComm*, 2015, **17**, 5690–5701; (*d*) Y.-Q. Huang, Y. Zhao, P. Wang, Y.-a. Okamura, B. N. Laforteza, Y. Lu, W.-Y. Sun and J.-Q. Yu, *Dalton Trans.*, 2017, **46**, 12430–12433; (*e*) S. Sen, N. N. Nair, T. Yamada, H. Kitagawa and P. K. Bharadway, *J. Am. Chem. Soc.*, 2012, **134**, 19432–19437.

12 (*a*) K. Vijay, C. Nandi and S. D. Samant, *RSC Adv.*, 2016, **6**, 49724–49729; (*b*) S. Chaudhary and M. D. Milton, *J.*

Photochem. Photobiol., A, 2018, **356**, 595–602; (*c*) S. Bishnoi and M. D. Milton, *J. Photochem. Photobiol., A*, 2017, **335**, 52–58.

13 R.-M. Wen, S.-D. Han, G.-J. Ren, Z. Chang, Y.-W. Li and X.-H. Bu, *Dalton Trans.*, 2015, **44**, 10914–10917.

14 S. Sen, N. N. Nair, T. Yamada, H. Kitagawa and P. K. Bharadaj, *J. Am. Chem. Soc.*, 2012, **134**, 19432–19437.

15 P. R. Edgington, P. McCabe, C. F. Macrae, E. Pidcock, G. P. Shields, R. Taylor, M. Towler and J. V. D. Streek, *J. Appl. Crystallogr.*, 2006, **39**, 453–457.

16 G. M. Sheldrick, *SADABS, Program for Empirical Absoption Correction of Area Detector Data*, University of Göttingen, Germany, 1996.

17 (*a*) G. M. Sheldrick, *SHELX-97, An Integrated System for Solving Crystal Structures from Diffraction Data*, University of Göttingen, Germany, 1997; (*b*) G. M. Sheldrick, *SHELX-97, An Integrated System for Refining Crystal Structures from Diffraction Data*, University of Göttingen, Germany, 1997.

18 G. M. Sheldrick, *SHELXTL, Version 6.10*, Bruker AXS Inc., Madison, Wisconsin, USA, 2000.

19 M.-C. Yin, L.-J. Yuan, C.-C. Ai, C.-W. Wang, E.-T. Yuan and J.-T. Sun, *Polyhedron*, 2004, **23**, 529–536.

20 M. Du, X.-H. Bu, Y.-M. Guo, H. Liu, S. R. Batten, J. Ribas and T. C. W. Mak, *Inorg. Chem.*, 2002, **41**, 4904–4908.

21 A. L. Spec, *J. Appl. Crystallogr.*, 2003, **36**, 7–13.

22 (*a*) H. Wang, L. Lyu, S. Zhang, J. Feng, R. Pang, L. Jiang, D. Li and C. Li, *Chin. J. Lumin.*, 2017, **38**, 1429–1435; (*b*) G. Blasse and A. Bril, *J. Chem. Phys.*, 1966, **45**, 3327–3332.

23 (*a*) M. A. Kesseler, *Anal. Chim. Acta*, 1998, **364**, 125–129; (*b*) J. R. Lakowicz, H. Szmacinski and M. Karakelle, *Anal. Chim. Acta*, 1993, **272**, 179–186; (*c*) H. Xu, H. C. Hu, C. S. Cao and B. Zhao, *Inorg. Chem.*, 2015, **54**, 4585–4587.

24 (*a*) B. Liu, W. Wu, A. Dou and Y. Wang, *Dalton Trans.*, 2015, **44**, 4423–4427; (*b*) J. Hao and B. Yan, *Chem. Commun.*, 2015, **51**, 7737–7740.